

Ultrafast narrowband exciton routing within layered perovskite nanoplatelets enables low-loss luminescent solar concentrators

Mingyang Wei^{1,5}, F. Pelayo García de Arquer^{1,5}, Grant Walters^{1,5}, Zhenyu Yang¹, Li Na Quan¹, Younghoon Kim^{1,2}, Randy Sabatini¹, Rafael Quintero-Bermudez¹, Liang Gao¹, James Z. Fan¹, Fengjia Fan¹, Aryeh Gold-Parker^{3,4}, Michael F. Toney³ and Edward H. Sargent^{1*}

In luminescent solar concentrator (LSC) systems, broadband solar energy is absorbed, down-converted and waveguided to the panel edges where peripheral photovoltaic cells convert the concentrated light to electricity. Achieving a low-loss LSC requires reducing the reabsorption of emitted light within the absorbing medium while maintaining high photoluminescence quantum yield (PLQY). Here we employ layered hybrid metal halide perovskites—ensembles of two-dimensional perovskite domains—to fabricate low-loss large-area LSCs that fulfil this requirement. We devised a facile synthetic route to obtain layered perovskite nanoplatelets (PNPLs) that possess a tunable number of layers within each platelet. Efficient ultrafast non-radiative exciton routing within each PNPL (0.1ps^{-1}) produces a large Stokes shift and a high PLQY simultaneously. Using this approach, we achieve an optical quantum efficiency of 26% and an internal concentration factor of 3.3 for LSCs with an area of $10 \times 10\text{cm}^2$, which represents a fourfold enhancement over the best previously reported perovskite LSCs.

Luminescent solar concentrators^{1,2} (LSC) consist of luminescent chromophores, such as organic fluorophores² or colloidal quantum dots (QDs)^{3,4}, embedded in a transparent waveguide. Broadband photons from incident sunlight are first absorbed by the chromophores, and are then emitted at a longer wavelength. The emitted photons are waveguided to solar cells attached on the perimeter of the waveguide panel where they are converted to electrical power. Solar concentration offers one path to increase efficiency at reduced cost, since high-efficiency solar cells can be then employed over areas that are smaller than the light collection area. This technology can also play a role in building-integrated photovoltaics in view of control over the colour and transparency of LSC films.

The optical quantum efficiency (OQE)¹, a key figure of merit for LSCs, is the ratio of the number of photons emitted from the panel edges to the total number of absorbed photons. To achieve a high OQE, the scattering loss of the LSC film should be minimized. In addition to maximizing the waveguide quality of the LSC film, it is essential to maximize photoluminescence quantum efficiency (PLQY) of the chromophores to achieve high OQE. A sufficiently large Stokes shift—the difference between the optical absorption band edge and the emission band wavelength—minimizes reabsorption of photons as they propagate through the waveguide.

In previous reports, large Stokes shifts have been engineered using strain-enhanced electron–phonon coupling and defect-induced subband states; unfortunately, these led to low PLQY³. Several strategies, including donor and acceptor mixes² with energy migration, indirect-bandgap QDs⁴ and engineered QDs with thick shells^{3,5} or impurity dopants^{6,7}, have been used successfully to combine an increased Stokes shift with a high PLQY to achieve high-performance LSCs. Today, OQEs as high as 24% and 18% for

100cm^2 device areas have been achieved for Stokes shift-engineered CdSe QDs⁵ and CISE/ZnS QDs⁸, respectively. We note that these performance levels leave further room for improvements through the PLQY, which remains below 70% and limits LSC overall performance (Supplementary Table 1).

We took the view that engineering energy transfer within highly luminescent materials could further enhance LSC performance. Metal halide perovskites are attractive luminescent materials in view of their ease of fabrication and excellent photoluminescence properties^{9,10}. These qualities are in principle ideal for LSC applications. However, the methods routinely used to engineer large Stokes shifts in other materials are not accessible in perovskites. There are no available methods to grow perovskite core–shell QDs, and doping strategies have resulted in low PLQYs^{11–14}. As a result, an OQE of only 7.5% has been reported for the leading perovskite LSC ($25\text{cm} \times 20\text{cm}$), which exploits Mn²⁺ dopants to suppress reabsorption¹⁴.

Layered, or quasi-two-dimensional perovskites, consist of sheets of three-dimensional perovskites sandwiched by bulky cations that divide the corner-sharing inorganic octahedral three-dimensional framework^{15–17}. The thickness of each layer is controlled through the proportion of methylammonium (CH_3NH_3^+ , MA) cations to the non-incorporating bulky cations. This results in a structure of formula $\text{R}_2(\text{MA})_{n-1}\text{Pb}_n\text{X}_{3n+1}$ (R = bulky cation, X = Cl/Br/I) where n represents the number of stacked inorganic sheets contained within one layer. In Supplementary Fig. 1, the crystal structure of an individual layered sheet is shown for the $n=2$ perovskite. Decreasing n increases the electronic bandgap and exciton binding energy due to quantum and dielectric confinement¹⁷. This concept has been utilized to make high-performance perovskite light-emitting diodes^{17–20}.

¹Department of Electrical and Computer Engineering, University of Toronto, Toronto, Ontario, Canada. ²Convergence Research Center for Solar Energy, Daegu Gyeongbuk Institute of Science and Technology, Daegu, Republic of Korea. ³Stanford Synchrotron Radiation Lightsource, SLAC National Accelerator Laboratory, Menlo Park, CA, USA. ⁴Department of Chemistry, Stanford University, Stanford, CA, USA. ⁵These authors contributed equally: Mingyang Wei, F. Pelayo García de Arquer, Grant Walters *e-mail: ted.sargent@utoronto.ca

We sought herein to engineer the dynamics of energy transfer in ensembles of quasi-two-dimensional perovskite nanoplatelets (PNPLs) for low-loss LSCs. Within PNPL ensembles, we observe tunable ultrafast energy transfer on picosecond timescales, and leveraged this to engineer a Stokes shift that minimizes reabsorption and maximizes the OQE. LSC devices were fabricated with PNPLs/poly(methyl methacrylate) composites coated on standard commercial glass. This system provides OQEs that reach 26% and internal concentration factors of 3.3 for $10\text{ cm} \times 10\text{ cm}$ panels. This improvement in internal concentration factor represents a fourfold enhancement compared with previously reported perovskite LSCs¹⁴.

Exciton routing in LSCs via layered perovskites

Ideally, layered perovskite ensembles offer the possibility of systematically controlling the Stokes shift while maintaining a high PLQY by adjusting the n values of the constituent layers. Typical solution-processed layered perovskites are ensembles of mixed n rather than single-phase layers¹⁷. These ensembles form a disordered system in which energy transfer^{17,19} occurs rapidly from low n layers (donors) to high n layers (acceptors). This materials platform, although attractive in principle, has thus far failed in attaining a high PLQY (Supplementary Fig. 2) when the donor/acceptor ratio is set to minimize reabsorption. This is a consequence of the difficulty in simultaneously controlling the distribution of layers and achieving the passivation required to minimize non-radiative recombination.

In contrast, PNPLs, the colloidal counterparts of solution-processed layered perovskite ensembles, are ideal for LSC applications since their composition can be tuned without sacrificing PLQY (Fig. 1a–c)^{21,22}. The tunability allows engineering of efficient energy transfer between the different phases, thus a large Stokes shift can be accompanied by a high PLQY²³.

To quantify design principles of PNPLs for LSC applications, we began by modelling the impact of reabsorption in the LSC architecture (see Supplementary Methods). For a given material configuration, trapping and photon escape on each successive radiation/absorption event can work against high performance in the presence of reabsorption (Fig. 1d). Depending on the number of reabsorption events, such effects can completely quench the OQE. Considering a typical escape probability of 0.25, as few as 10 reabsorption events suffice for a photon to be lost with a probability higher than 0.95. The simultaneous achievement of low reabsorption and minimized carrier trapping is therefore required to attain high quantum yield and high OQE.

We thus reasoned that, for this approach to be effective, efficient energy transfer to the final acceptor phase needs to take place non-radiatively. Throughout the process, a distribution of narrowband donors and acceptors is also crucial in preventing reabsorption. Such narrowband exciton routing would ensure that energy is rapidly concentrated in the final acceptor emitter via non-radiative channels at a rate that would need to outpace charge trapping kinetics and then can be radiatively emitted into the waveguide.

The maximum available exciton concentration factor—the increase in the exciton density in the acceptor on funnelling—can be estimated as a first approximation from the ratio of acceptor to donor phases. Low acceptor concentrations will cause a high fraction of excitons to not be able to find an acceptor state before their energy is lost in traps, or emitted into the escape cone, lowering thereby the exciton concentration factor (Fig. 1e). As the acceptor concentration increases, more excitons are likely to find an acceptor state, but this is at the expense of reducing exciton concentration and increasing reabsorption. An optimum acceptor concentration maximizes OQE for each material/energy configuration (Fig. 1f).

Structural properties of PNPLs

Based on these considerations, we sought to synthesize narrowband quasi-two-dimensional PNPLs with a tunable phase composition and efficient energy transfer. PNPLs were formed by diluting

perovskite precursors into antisolvent^{21,22}. By controlling the relative proportion of methylammonium bromide (MABr) and hexylammonium bromide (HABr)²², we obtain PNPLs consisting of dominant single phases ($n=1, 2, 3$), or of several intermixed phases with a controllable distribution. This constitutes the basis system for structural characterization and composition engineering.

Grazing incidence wide-angle X-ray scattering (GIWAXS) measurements reveal the layered nature of the perovskite platelets (Fig. 2a). A series of periodically spaced reflections stemming from the periodicity of the layered structures along their c axis^{24,25} were observed from the PNPL films assembled via centrifugal casting (Fig. 2b). The peaks are found mainly along q_z ($q_{xy}=0$), showing that their c axis is normal to the substrate, which may be related to the centrifugal casting. Interlayer separations of $d=18.5\text{ \AA}$, 24.2 \AA and 29.9 \AA were found for $n=1$, $n=2$ and $n=3$ films from the first-order peak, respectively. Diffraction peaks for $n=1$ are present in the nominal $n=2$ film, and peaks for $n=1$ and $n=2$ are observed in the nominal $n=3$ film, showing the presence of minority fractions of additional phases in the PNPLs. These data also indicate that, in the PNPLs that show co-existence of different n layers, there exists significant strain: $d(001)$ of $n=1$ and $n=2$ is smaller when higher n species coexist with $n=1$ and $n=2$ layers, respectively (Supplementary Table 2). Absorption and luminescence spectroscopies reveal strong exciton features in these structures (Fig. 2c), with a tunable bandgap in the blue region of the spectrum and narrowband emission.

Transmission electron microscopy (TEM) and atomic force microscopy (AFM) further reveal the structure of individual PNPLs. For PNPLs composed of $n=2$ and $n=3$ layers (Supplementary Fig. 3a), lateral dimensions varying between 100 nm and 500 nm were found for individual PNPLs based on TEM and AFM images (Supplementary Fig. 3b,c). Typical thicknesses of about 20 nm were obtained from the height profile of AFM images (Supplementary Fig. 3d), which is much larger than the thickness of single $n=2$ and $n=3$ layers. Combined with the consistent orientation of different layers and the strain in mixed n films observed in GIWAXS, this indicates that individual PNPLs consist of several stacked layers, a fact that enables the co-existence of different n phases within a single platelet. We offer that this layer stacking may lead to fast concentration of excitons into the lower-bandgap phases within individual PNPLs. We note that this is especially critical in achieving high exciton concentration factors, as typical LSCs consist of nanoparticles separated by a polymer host, where non-radiative energy transfer among nanoparticles is inefficient.

Ultrafast energy transfer in PNPLs

To verify that efficient energy transfer can occur in PNPLs/polymer composites, which is crucial for fabricating a low reabsorption LSC, we characterized energy migration in mixed-phase PNPLs with the aid of ultrafast transient absorption spectroscopy (Fig. 3). The pump intensity was kept below the threshold of Auger recombination (Supplementary Fig. 4). Purest- n PNPL films were first analysed to exclude any fast processes within single-phase layers that might obscure the transfer study (Supplementary Fig. 5). We then synthesized PNPLs consisting of $n=2$ and $n=3$ phases, and deposited them via centrifugal casting. This ensured that the PNPLs were closely packed within the film. Ground-state bleaching (GSB) peaks were found at 430 nm ($n=2$) and 450 nm ($n=3$) (Supplementary Fig. 6c,d), corresponding well with the linear absorption of the films (Supplementary Fig. 6a).

A key test of energy transfer is to witness an accelerated decrease in the donor GSB accompanied by an increase in the acceptor GSB on increasing acceptor inclusions. When we increase the ratio of acceptor $n=3$ phases in the system (Supplementary Fig. 6b), the decay rate of the donor $n=2$ bleach at 430 nm increases from 0.02 ps^{-1} to 0.1 ps^{-1} (Fig. 3a). The complementary trend is

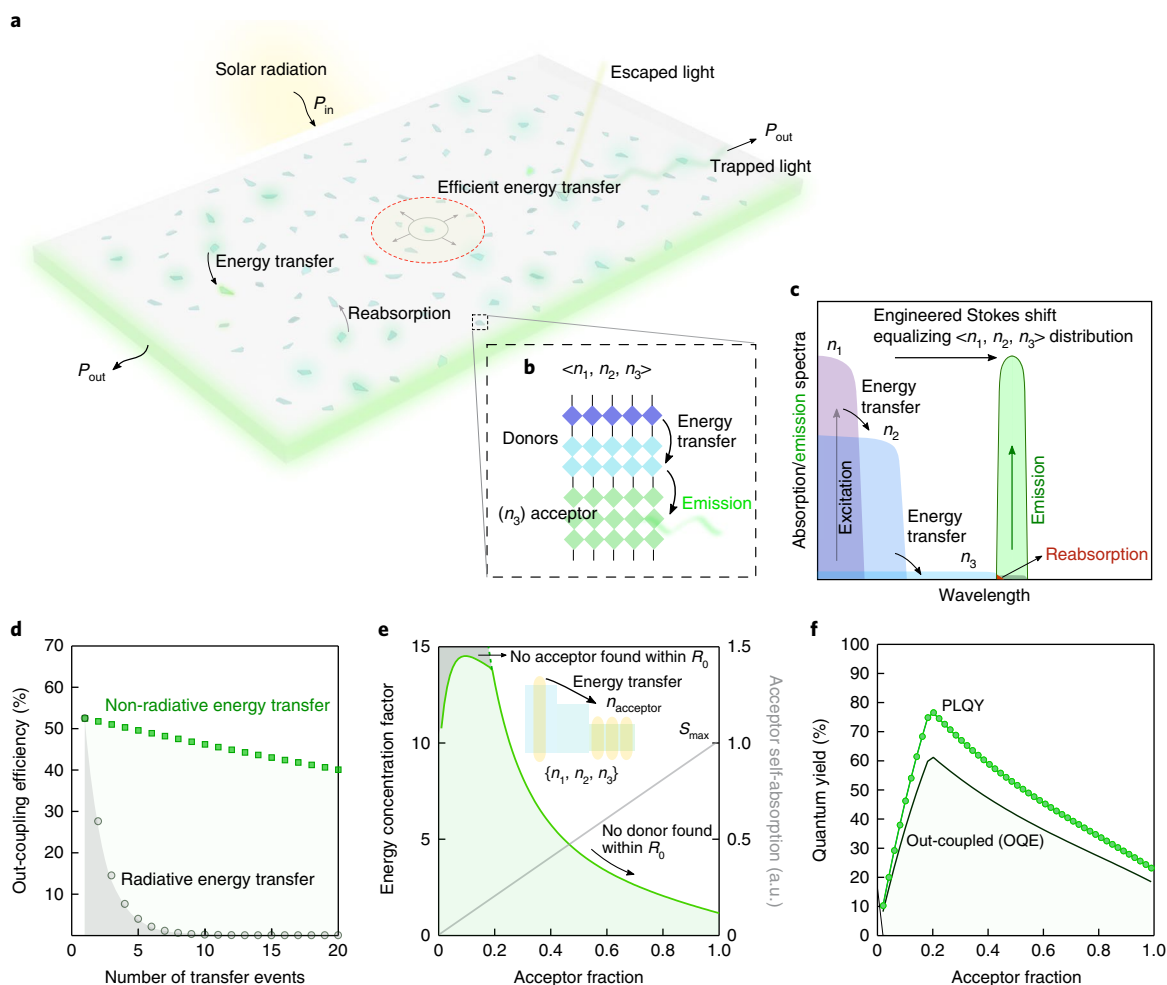


Fig. 1 | Design principles of efficient LSCs based on ultrafast narrowband exciton routing. **a**, A LSC is composed of bright chromophores embedded in a transparent waveguide matrix. Solar irradiation with a power P_{in} is absorbed in the chromophores (in our case, layered perovskite nanoplatelets) and partially re-emitted to the edge of the waveguide with a power P_{out} . **b**, Illustration of the energy transfer process within layered perovskite platelets composed of donor phases n_1 , n_2 and acceptor phase n_3 . Mixed-phase layered perovskites enable manipulation of the energy landscape, directing excitons to the narrower-bandgap components. **c**, This allows engineering of large Stokes shifts, minimizing reabsorption and maximizing photoluminescence quantum yield. **d**, Radiative energy transfer events can quench the out-coupling efficiency in LSCs via photon escape. Non-radiative ultrafast energy transfer improves exciton routing to the final acceptor subpopulation and allows efficient energy focusing. **e**, Energy concentration factor, defined as the increase in the exciton density in the acceptor phase compared with in a single-phase scenario; and acceptor self-absorption, as the acceptor fraction varies. Rapid exciton accumulation happens only within acceptors found within the Förster radius (R_0) of an exciton. When the acceptor fraction is too high, no donor is found within R_0 of the acceptor to enable energy transfer, and the energy concentration factor also decreases. The acceptor self-absorption reaches the maximum value S_{max} for the acceptor-only system. Inset: exciton (yellow rectangles) concentration process from the donor phases to the acceptor phase via energy transfer. **f**, An optimum acceptor concentration will exist that maximizes the out-coupling efficiency. Calculation details can be found in Supplementary Methods.

monitored at the acceptor GSB wavelength (450 nm), with increase rates of 0.03 ps^{-1} and 0.1 ps^{-1} , respectively (Fig. 3b). These energy transfer rates significantly exceed those of donor–acceptor mixes of organic fluorophores^{26,27} and QDs^{28,29}, which span several hundred picoseconds to nanoseconds. The ultrafast transfer rates observed in the closely packed PNPLs film indicates that energy transfer from the donor to the neighbouring acceptor layers is efficient.

We then diluted the PNPLs in a polymer host matrix of polystyrene to study the energy transfer rate and mechanism in an LSC system. First, inter-PNPL energy transfer was evaluated by mixing pre-synthesized $n=2$ PNPLs with $n \geq 3$ PNPLs (Supplementary Fig. 7a,b) in a polystyrene matrix at different concentrations (Fig. 3c), which separates $n=2$ NPLs from acceptor layers spatially. We found that, in this case, no energy transfer is detected for the $n=2$ GSB trace, which overlaps with that of the pure $n=2$ NPLs/

polystyrene film. This implies that energy transfer does not occur efficiently unless different layers are stacked closely.

The energy transfer rate of one-step-synthesized mixed $n \geq 2$ phase PNPLs was then measured at different concentrations (Supplementary Fig. 7c) in the polystyrene matrix (Fig. 3e). A constant decay rate of around 0.015 ps^{-1} was found for the $n=2$ GSB that did not significantly vary for concentrations below 0.013 weight/weight (w/w) PNPL to polystyrene matrix ratio. This is much faster than pure $n=2$ films, which exhibit a decay of 0.003 ps^{-1} , demonstrating energy transfer within PNPLs in the polystyrene matrix. We ascribe the ultrafast rates in our PNPLs within polystyrene matrices to being possible due to intimate stacking of donor and acceptor layers within individual platelets.

This evidence shows that the mixed n phase PNPLs in a polymer waveguide has ultrafast energy transfer within different layers of the

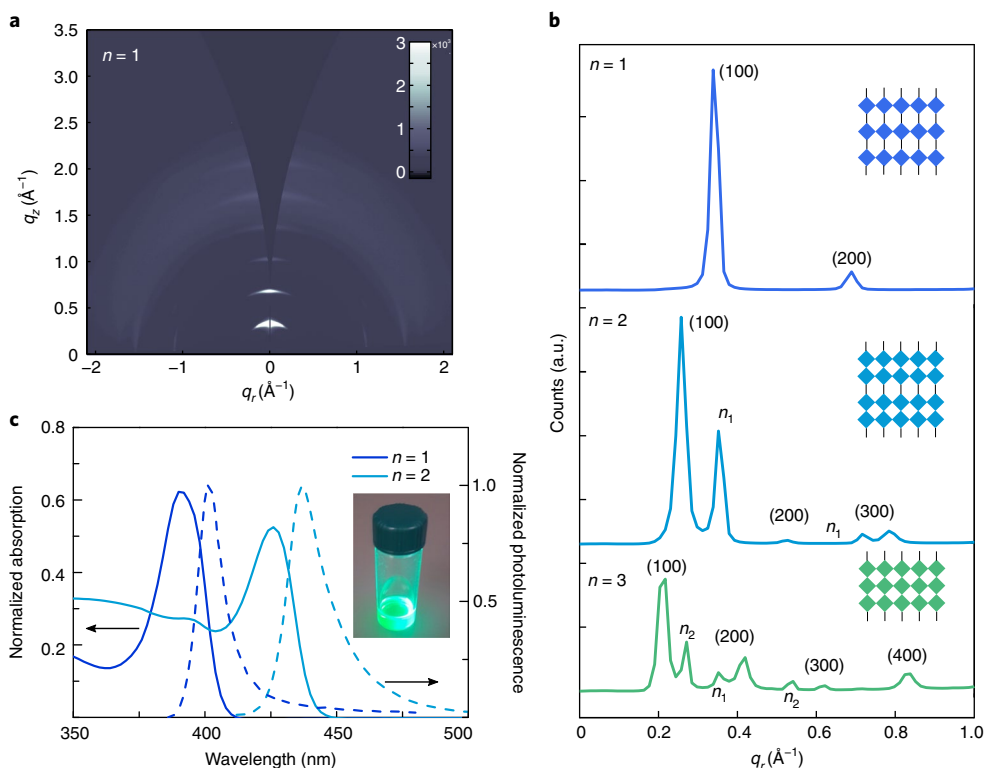


Fig. 2 | Synthesis and material properties of single-phase layered PNPLs. **a**, GIWAXS of $n=1$ platelet films shows a strong orientation of the c axis normal to the substrate. The colour bar shows the diffraction intensity collected from the GIWAXS detector. q_r and q_z represent in-plane and near out-of-plane scattering vectors, respectively. **b**, Cuts near the q_z axis of the GIWAXS show different peaks associated with phases corresponding to $n=1, 2, 3$ for the purest $n=1, n=2$ and $n=3$ film. Insets: illustration of the structure of $n=1, n=2$ and $n=3$ nanoplatelets, respectively. **c**, The absorption spectra (solid line) and emission spectra (dotted line) of $n=1$ and $n=2$ reveal the effect of quantum confinement: a blueshift in absorption band edge and photoluminescence bandgap with decreasing n . Inset: a photograph of PNPL solution under ultraviolet illumination.

layered perovskites. In a LSC system, this mechanism enables the potential for reabsorption suppression.

Reabsorption reduction by composition tuning

Encouraged by the ultrafast non-radiative energy transfer within PNPLs, we then sought to optimize the composition distribution within PNPLs to minimize reabsorption. We leveraged the control over the phase distribution enabled by our synthesis method, and fabricated PNPLs composed of $n = \{2, 3, 4, 5\}$ phases by tuning the perovskite precursor ratio. Specifically, we fixed the ratio of PbBr_2 , MABr and HABr in the precursor mix to 3:2:2 x and modified x to modulate the phase distribution and the final Stokes shift.

As the relative amount of HABr increases, the band edge absorption of PNPLs is reduced, indicating a reduced proportion of acceptor phases in the film, which in turn facilitates reducing the absorption–emission overlap coefficient (S) (defined in Fig. 4a) (Fig. 4a,b). We quantified the relative presence of acceptor phases by calculating the ratio of the areas of the lowest energy GSB to the total area of bleach signals as

$$\eta_{\text{acceptor}} = \frac{\int_{\text{lowestGSB}} \Delta A dE}{\int_{\text{allGSBs}} \Delta A dE} \quad (1)$$

where ΔA and dE represent the film absorption change after pumping and the differential of photon energy, respectively. We found that η_{acceptor} reduces from 50% to 30% as x varies from 0.8 to 1.0 (Supplementary Fig. 8a). The absorption–emission overlap factor also follows this trend (Fig. 4b). For $x > 1.1$ (acceptor

concentration < 30%), the acceptor concentration further decreases, while the absorption–emission overlap is not further reduced.

We then drop-cast PNPLs/polystyrene composites with different η_{acceptor} on a 2.5 cm × 2.5 cm glass slab and characterized the associated optical loss changes. For optical loss evaluation, we measured the PLQY of composite films before ($\text{PLQY}_{\text{total}}$) and after ($\text{PLQY}_{\text{surface}}$) covering the edges with opaque material as the η_{acceptor} varies (Fig. 4c). We then obtained the edge coupling efficiency:

$$\eta_{\text{edge}} = \frac{\text{PLQY}_{\text{total}} - \text{PLQY}_{\text{surface}}}{\text{PLQY}_{\text{total}}} \quad (2)$$

The $\text{PLQY}_{\text{total}}$ remains above 75% for $x < 1.2$, better than that of Stokes shift-engineered QDs (<70%)^{3,5}. As a result of reduced self-absorption, η_{edge} reaches a maximum of 60% as x is increased from 0.8 to 1.0 (Fig. 4c). As the fraction of the acceptor domains further diminishes, excitons cannot be routed to the final acceptor before being lost via trapping or successive reabsorption events (Fig. 1e). This fact causes η_{edge} and PLQY to drop for $x > 1.1$. This trend is in good agreement with analytical simulations whose input parameters are obtained from experimental materials measurements (Fig. 1f and Supplementary Methods).

To further confirm that the η_{edge} variation is a result of changes in reabsorption loss, we evaluated the waveguide quality of the film by recording the propagation loss of 634 nm laser light passing through films of different lengths (Fig. 4d). The photoluminescence intensity remains 95% of the original value for an optical path of 3 cm, which is also close to that for the bare glass slab. Here, the maximum

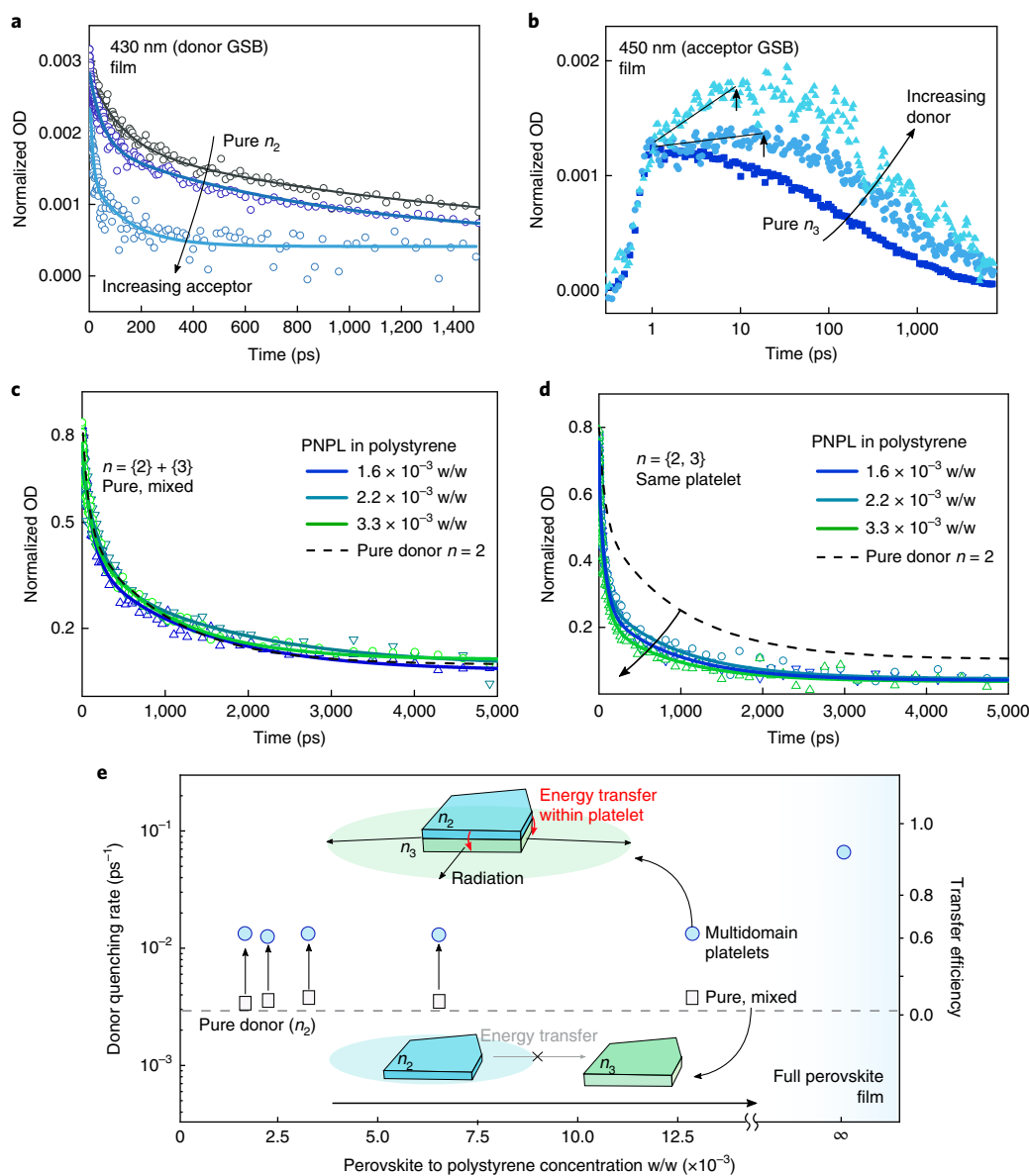


Fig. 3 | Ultrafast energy transfer in multiphase layered PNPLs. **a,b**, Transient absorption spectral dynamics for different of $n = \{2, 3\}$ PNPLs at the donor (**a**) and acceptor (**b**) GSB traces. OD represents optical density. The donor traces are extracted from the transient absorption spectra of the purest $n = 2$ film (black dot) and films with $n = \{2, 3\}$ distribution A (sky-blue dot) and B (blue dot) (defined in Supplementary Fig. 6), respectively, and the acceptor GSB traces are extracted from the purest $n = 3$ film (blue dot) and films with $n = \{2, 3\}$ distribution C (sky-blue dot) and D (cyan dot) (defined in Supplementary Fig. 6), respectively. The donor traces are fitted using a biexponential decay function. Energy transfer is evidenced by the accelerated quenching at the donor and the increasing signal and decay time at the acceptor. **c,d**, Decay of the GSB band at 430 nm when the separately synthesized $n = 2$ and $n = 3$ PNPLs (**c**) or mixed-phase $n = \{2, 3\}$ PNPLs (**d**) are embedded into the host polystyrene matrix with different w/w ratios. In the PNPLs/polystyrene waveguide, efficient energy transfer only occurs if different phases coexist within the same platelet. The data are fit using a biexponential decay function. **e**, Donor quenching rate and estimated transfer efficiency within multiphase NPLs (blue circles) and pure-phase NPLs (white squares), as a function of the concentration of the PNPLs in the polystyrene matrix. Intra-platelet energy transfer is observed in the polystyrene matrix (top inset), while inter-platelet energy transfer is avoided (bottom inset) as a result of spatial separation of different NPLs in the polystyrene matrix.

η_{edge} is around 80% of the theoretical upper limit⁵ ($\eta_{\text{edge,limit}} = 75\%$), suggesting the scattering loss and absorption loss of the photoluminescence to the η_{edge} variation is small.

PNPL for low-loss large-area LSCs

We used $x = 1.0$ NPLs for LSC fabrication since they exhibited the lowest reabsorption losses in a polymer matrix. Poly(methyl methacrylate) (PMMA) was chosen as the polymer host because its low absorption coefficient³⁰ is necessary for producing low-loss

large-area LSCs. Perovskite LSCs were fabricated by depositing a mixture of PNPLs and PMMA in chlorobenzene onto glass substrates by rod coating (see Methods). For comparison, $\text{CH}_3\text{NH}_3\text{PbBr}_3$ perovskite QDs (PQDs) were synthesized and used for LSC fabrication. The largest LSC fabricated has a size of $10 \text{ cm} \times 10 \text{ cm} \times 0.2 \text{ cm}$, with a geometric gain factor G ($G = \text{Area}_{\text{front}} / \text{Area}_{\text{edges}}$) of 12.5, which is among the largest gain factors of LSCs reported^{5,6}.

The photoluminescence and absorption spectra of the LSC film with PNPLs and PQDs are shown in Fig. 5a. Here we define the LSC

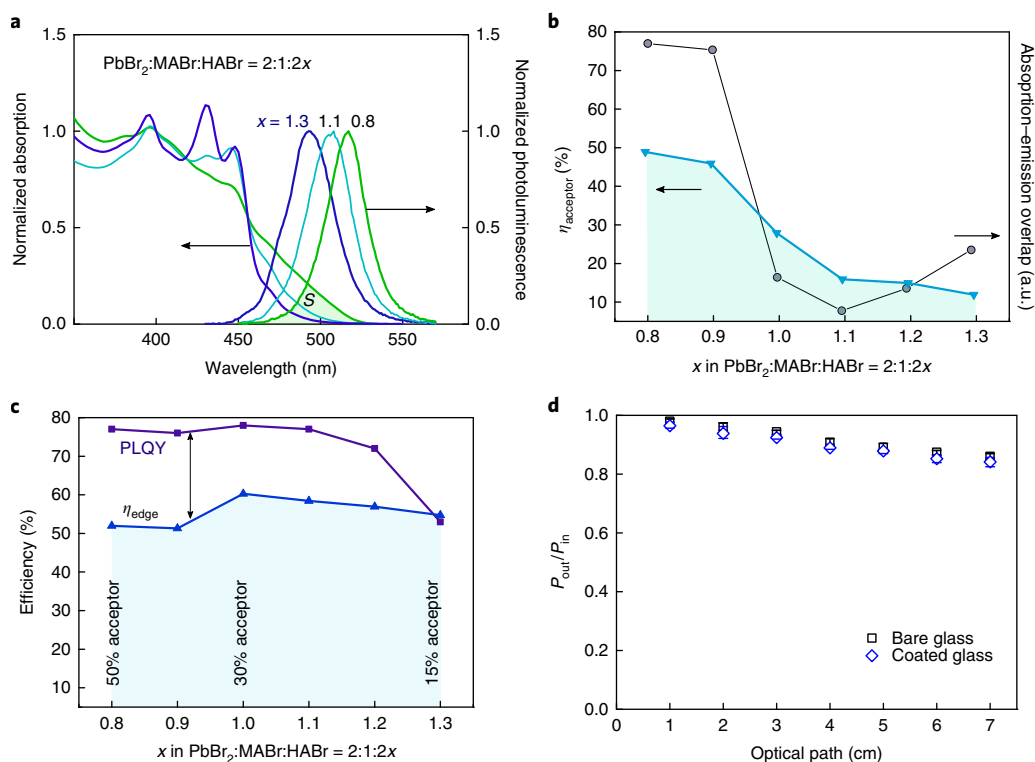


Fig. 4 | Modification of donor/acceptor ratios to reduce reabsorption loss. **a**, Absorption and emission spectra of LSCs of PNPLs composed of different stoichiometries $n = \{2, 3, 4, 5\}$ by varying the molar concentration of PbBr_2 , MABr and HABr in the precursor mix according to the ratio 3:2:1:2x (see Methods). The absorption near the band edge can be controlled in such a way that reabsorption is decreased. The green shaded area represents the absorption-emission overlap (S). **b**, The absorption-emission overlap coefficient (S), defined as the overlapping area of the absorption spectra and photoluminescence spectra, and relative presence of the final acceptor as the stoichiometry changes. **c**, PLQY (purple dots) and OQE (blue triangles) as a function of stoichiometry. An optimized edge out-coupling efficiency of 60% is obtained for the acceptor concentration $\eta_{\text{acceptor}} \sim 30\%$. **d**, Propagation loss of 633 nm laser as a function of optical length. Output power (P_{out}) retains 95% of the input power (P_{in}) for an optical length of 3 cm, suggesting a high waveguide quality of the film.

quality factor Q_{LSC} as the ratio of the absorbance at 400 nm and the absorption at the photoluminescence emission wavelength to compare the spectral overlap. As shown in Supplementary Fig. 9, Q_{LSC} at the photoluminescence peak is 15.7 for PNPLs while, for PQDs, Q_{LSC} is 5.7. As reported before, the internal concentration factor C_{int} ($C_{\text{int}} = G \times \text{OQE}$) will not be saturated for optical paths up to 50 cm with a Q_{LSC} of 10 and a PLQY of 90% (ref. 31). As a result, high OQE was expected for the 10 cm \times 10 cm NPLs LSC. A photograph of the 10 cm \times 10 cm NPLs LSC is provided in Fig. 5b.

The optical loss of PNPL- and PQD-based LSCs was evaluated by measuring the photoluminescence spectra from the waveguide as a function of optical path achieved by varying the excitation-collection distance. Here reabsorption is the dominant loss channel as revealed by the high-quality waveguide formed with the PNPLs/polymer film (Fig. 4d). Reabsorption loss was both evidenced by photoluminescence loss (Fig. 5c and Supplementary Fig. 10), especially in the blue side of the photoluminescence spectra as well as the continuous decay of the integrated photoluminescence intensity as the optical length increases (Fig. 5d). However, the absorption in the red side of the photoluminescence spectra for PNPLs is considerably smaller when compared with the PQDs. The integrated photoluminescence intensity can retain 50% at 6 cm optical length when compared with the 1.5 cm optical length; while for PQDs, the propagation loss is over 85%. Herein we confirm that the reabsorption of the engineered PNPLs is sufficiently small to enable low-loss LSCs.

PNPL LSC performance was measured for device areas ranging from 2 cm \times 2 cm to 10 cm \times 10 cm with an excitation wavelength of 400 nm as shown in Fig. 5e. From integrating-sphere

photoluminescence measurements, the average PLQY and OQE decreases as the LSC length increases from 2 cm to 5 cm. This mainly comes from the reabsorption loss as the waveguide quality is high. In detail, the average PLQY dropped from 81.6% (2 cm \times 2 cm) to 68.7% (5 cm \times 5 cm). Similarly, OQE dropped from 51.2% to 38.5%. The increased reabsorption was also seen by the larger spectral loss in the blue side of photoluminescence spectra when the device area is larger (Supplementary Fig. 11a,b). In addition, the OQE remained above 48% for multiple choices of excitation wavelength for the 2 cm \times 2 cm film (Supplementary Fig. 11c): thus, the high performance of the perovskite LSCs is maintained over a broad range of the incident photon energies.

To evaluate the potential of perovskite LSCs for real-life applications, electro-optical measurements were conducted for the 10 cm \times 10 cm area LSC film under outdoor conditions. Here we recorded the photocurrent of a taped solar cell with and without attachment to the edge of an LSC film (I_{LSC} and I_{PV} , respectively). Visual information of this LSC/photovoltaic system is shown in Supplementary Fig. 12. Here $I_{\text{LSC}}/I_{\text{PV}}$ is 18.9% and 17.8% (Supplementary Fig. 13c,d) for two samples fabricated and measured independently. Consequently, the OQE is 26.2% and 24.6% respectively (Supplementary Note 1). An internal concentration factor of 3.3 achieved for the 10 cm \times 10 cm perovskite LSCs, herein, represents a nearly fourfold enhancement compared with the best-performing perovskite LSC ($C_{\text{int}} = 0.83$)¹⁴. As a complement to the outdoor measurements, we also measured LSC performance under 100 mW cm^{-2} AM 1.5G illumination, $I_{\text{LSC}}/I_{\text{PV}}$ is 18% under these conditions (Supplementary Fig. 14). This corresponds to an

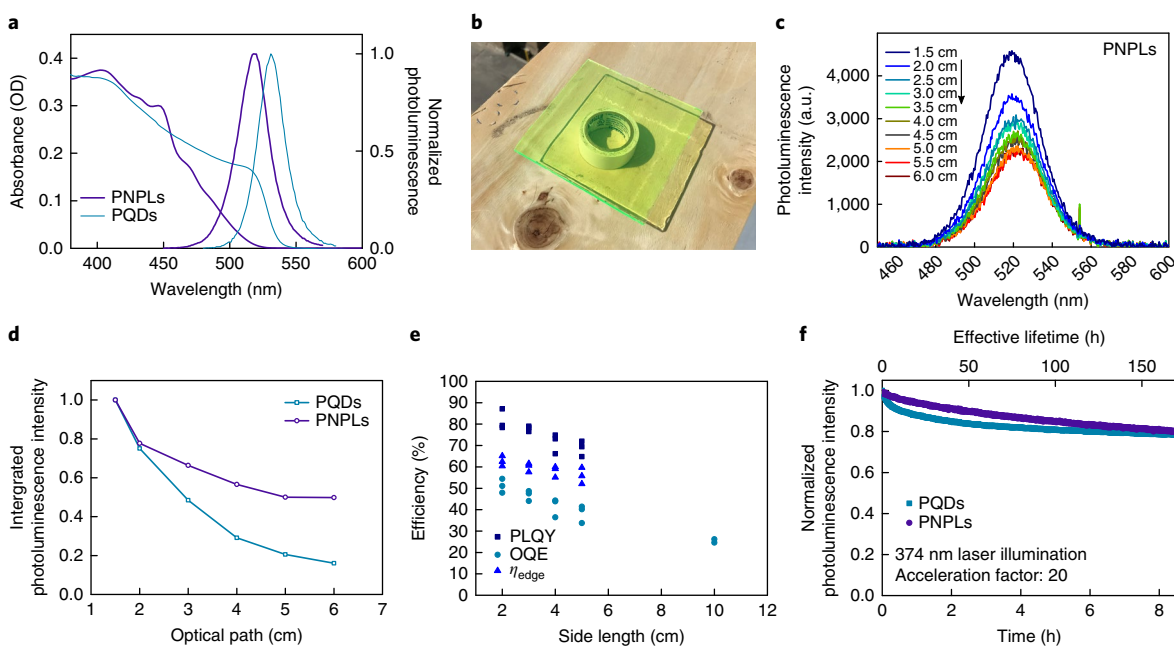


Fig. 5 | Ultrafast exciton routers enable low-loss large-area perovskite LSCs. **a**, Absorption and emission spectra of LSCs of perovskite NPLs and QDs. Spectral overlap is greatly reduced for PNPLs compared with QDs. **b**, Photograph of a 10 cm × 10 cm PNPL-based LSC. **c**, Photoluminescence spectra of perovskite NPLs emerging from the LSC edge as a function of the distance between the excitation spot and the collection edge. Reabsorption in the blue side of the spectra is observed. **d**, Spectrally integrated intensity of photoluminescence collected at the LSC edge as a function of propagation length. Stronger photoluminescence losses are observed for PQDs. **e**, The PLQY, edge coupling efficiency and the OQE of the square PNPL LSC as a function of LSC side length. From 2 cm × 2 cm to 5 cm × 5 cm device area, optical measurements are conducted. For each area, three independent measurements were carried out and their results are displayed in the panel as a function of side length. For the 10 cm × 10 cm device area, an electro-optical method was utilized (see Methods) to obtain two independent measurements. **f**, An accelerated light-soaking stability test of perovskite LSCs. The excitation source is a 374 nm laser diode, which corresponds to an acceleration factor of 20.

OQE of 25%, and thus agrees well with the outdoor measurements. We reason that the high OQE is a combination effect of high PLQY and relatively low reabsorption losses, as Stokes shift-engineered CdSe QDs and CISE QDs have lower PLQY (<70%) even though they exhibit higher Q_{LSC} compared with PNPLs^{31,32}.

The external optical quantum efficiency η_{ext} ($\eta_{\text{ext}} = \eta_{\text{abs}} \times \text{OQE}$), which is defined as the ratio of the number of photons emitted from the panel edges to the total incident photons, is 0.87%. The decrease in efficiency is associated with the appreciable transparency to visible light. Thus the current perovskite LSC is favourable for use in highly transparent solar windows. To work as a high η_{ext} solar concentrator/photovoltaic system, it will be necessary to achieve further reductions in the absorption onset energy of the PNPLs. As MAPbI₃ and MASnI₃ have bandgaps as low as 1.6 eV and 1.3 eV respectively, developing lead iodide- and tin iodide-based PNPLs is of interest towards this goal³.

The PNPL LSCs exhibited stability comparable to the QD LSCs: T_{80} (time after photoluminescence intensity has dropped to 80% of the initial intensity) of the QD and PNPL LSCs was 6.0 h and 8.5 h, respectively, measured under accelerated aging tests by exposing the LSC film to a 374 nm laser diode. This translates into 120 h and 170 h T_{80} under continuous light soaking of the standard outdoor conditions. (Fig. 5f). PNPL LSCs also exhibit good thermal and water stability, attributed to the combination of the polymer host protection and PNPL stability. Minimal degradation of LSCs was observed after we subjected the samples to temperature stress and water (80 °C or immersion in water for 8 h, Supplementary Fig. 15a).

Conclusions

This work demonstrated large-area and efficient LSCs that rely on narrowband exciton routing. Computational studies revealed that a

tailored exciton energy landscape can be used to overcome the most acute limitation of LSCs, reabsorption. In a system composed of different narrowband energy levels, excitons are non-radiatively routed to a small fraction of bright emitting states, where light will be emitted and efficiently coupled to the LSC edges minimizing additional reabsorption events. We developed a synthetic route to fabricate layered PNPLs with a tunable number of different n phases within a single platelet that maintained narrowband emission. We performed transient energy transfer studies that revealed ultrafast energy transfer rates, in the range of 0.01 to 0.1 ps⁻¹, within individual PNPLs. PNPL-based LSCs using PMMA as the polymer host on a standard glass slab was fabricated. The benefits of narrowband exciton routing are further evidenced for large-area LSCs (10 cm × 10 cm), where we achieved an OQE of 26% and an internal optical concentration factor of 3.3. This surpasses the performance of the best perovskite LSCs by a factor of four. The structural and chemical stability of PNPLs result in LSCs with good stability in time, temperature and under exposure to water. The narrowband exciton routing strategy contributes a facile, scalable route to the field of low-loss LSCs.

Methods

Materials. Lead bromide (PbBr₂, 99.9%) was purchased from Alpha Aesar. *N,N*-dimethylformamide (DMF, 99.8%), chlorobenzene (99.8%), acetonitrile (99.8%), oleic acid (>99%), oleylamine (>98%), PMMA (molecular weight ~120,000 by gel permeation chromatography) and polystyrene (average molecular weight 35,000) were purchased from Sigma-Aldrich. Methylammonium bromide (MABr), phenylethylammonium bromide (PEABr) and hexylammonium bromide (HABr) were purchased from Dyesol. All chemicals were used as procured without further purification.

Layered perovskite thin-film fabrication. The quasi-2.5-dimensional perovskite precursors were prepared by dissolving specific stoichiometric quantities of PbBr₂, MABr and PEABr in DMSO solvent. The resulting solution was filtered

using a PTFE syringe filter (0.2 μm) before deposition. The precursor solution was deposited to the substrate via a consecutive two-step spin-coating process at 1,000 r.p.m. and 5,000 r.p.m. for 10 and 60 s, respectively. During the second spin step, 100 μl of chloroform were deposited onto the substrate. The resulting films were then annealed at 90 °C for 10 min in a N_2 -filled glovebox.

Perovskite nanoplatelet synthesis. PbBr_2 , MABr and HEABr were dissolved in DMF while fixing the concentration of PbBr_2 at 0.06 M. Molar ratios of PbBr_2 , MABr and HABr were varied to control domain distributions. Then 20 μl of stock precursor solution was dipped into 1 ml of chlorobenzene that had already dissolved polystyrene in advance under concentrations of 0, 50, 100, 200, 300, 400 mg ml^{-1} under vigorous stirring, to immediately form PNPLs. PNPL films without polystyrene were formed via centrifugal casting. PNPL films with polystyrene were formed by drop-casting PNPL solution on a clean glass substrate and dried under vacuum for 3 h.

PQD synthesis. First, 55 mg of PbBr_2 and 30 mg of MABr were dissolved in 1 ml DMF. Then 25 μl of oleylamine and 300 μl of oleic acid were added in the solution. Then 20 μl of stock precursor solution was dipped into 1 ml of chlorobenzene under vigorous stirring, to immediately form PQDs. Then 1 ml of acetonitrile was added to the solution and the mixture was centrifuged at 8,000 r.p.m. for 15 min. The precipitate was dissolved by 1 ml chlorobenzene again. Then 1 ml solution was mixed with 1 ml PMMA solution (400 mg ml^{-1} in chlorobenzene) to form the composites for film coating.

Absorption measurements. Optical absorption spectra were measured with a Perkin Elmer 950 UV/VIS/NIR spectrometer equipped with an integrating sphere for thin-film measurements.

AFM measurements. AFM measurements were done with an Asylum Research Cypher operating in tapping mode with an AC240TM-R3 probe.

Transient absorption measurements. A regeneratively amplified Yb:KGW laser at a 5 kHz repetition rate (Light Conversion, Pharos) was used to generate femtosecond laser pulses, and a pulse picker was used to lower the frequency to 1 kHz. A portion of the 1,030 nm fundamental was sent into an optical bench (Ultrafast, Helios), where it passed through a retroreflector, and was then focused into a calcium fluoride crystal, translated at 1 mm s^{-1} , to create the white light continuum probe. An optical parametric amplifier (Light Conversion, Orpheus) was used to generate the 375 nm pump pulse by upconversion of the fundamental wavelength. This was then sent to the optical bench and was chopped at 500 Hz. Both the pump and probe were sent to the sample, with the time delay adjusted by changing the path length of the probe (time resolution \sim 350 fs). The probe pulse was then collected by a CCD after dispersion by a grating spectrograph (Ultrafast). Kinetic traces were fit to the convolution of the instrument response and a sum of exponential decays. Time zero was allowed to vary with wavelength to account for the chirp of the probe.

Fabrication of LSCs. To prepare PMMA and PNPL compositions, 1 ml of acetonitrile was added in 4 ml PNPL ($x = 1.0$)/chlorobenzene solution. The mixed dispersion was then centrifuged at 8,000 r.p.m. for 15 min. The precipitate was re-dispersed in 1 ml of chlorobenzene containing 2 μl of oleic acid and 0.2 μl of oleylamine (obtained by mixing chlorobenzene with 50 $\mu\text{l ml}^{-1}$ oleic acid and 5 $\mu\text{l ml}^{-1}$ of oleylamine solution in chlorobenzene) to avoid NPL aggregation. The dispersed NPL solution was then mixed with 1 ml of PMMA solution (400 mg ml^{-1} in chlorobenzene, dissolved by heating and stirring at 60 °C) and stirred for 1 h to yield homogenous composites.

Then 5 ml of composites was poured onto a glass substrate (10 $\text{cm} \times 10 \text{ cm}$) to form a strip in front of a glass rod. The rod was swiftly translated over the substrate to form a uniform solution film. The film was dried under vacuum for 20 min to fully remove all the solvent. After that, a highly uniform film was formed for further characterization. For small area substrates (from 2 $\text{cm} \times 2 \text{ cm}$ to 5 $\text{cm} \times 5 \text{ cm}$), composites were directly drop-casted on the substrate, and dried under vacuum following the same procedure.

Photoluminescence measurements. Photoluminescence measurements were performed using a Horiba Fluorolog system. Steady-state photoluminescence was collected by illuminating the samples with a monochromatized Xe lamp. PLQY measurements were done by coupling a Quanta-Phi integrating sphere to the Fluorolog system with optical fibre bundles. Both excitation and emission spectra were collected for the two cases of the sample directly illuminated by the excitation beam path in the integrating sphere and the empty sphere itself. The PLQY measurements were done by setting the Fluorolog to an excitation wavelength ranging between 360 nm to 440 nm and to have a 2 nm bandpass for both the excitation and emission slits. With these settings, the ensuing spectra had high signal-to-noise ratios and delivered an excitation intensity in a range of 1 mW cm^{-2} to the sample. The excitation intensity was calculated by measuring the power with an Ophir LaserStar Dual Channel Power and energy meter and calculating the beam area through the known dispersion relations for the monochromator. Excitation intensity spectra were collected with a calibrated neutral density filter

with known transmission placed after the integrating sphere. A Newport white light source was used to calibrate the detector and integrating sphere for the spectral variance. OQE was obtained by subtracting PLQY of the film with edges clear from PLQY of the film with edges blocked by black carbon paint.

***J-V* measurements on perovskite LSCs.** Polycrystalline silicon (c-Si) solar cells (500 $\text{mA}/0.5 \text{ V}$, Solar Made) with an area of 2.5 $\text{cm} \times 5 \text{ cm}$ were used for LSC characterization. External quantum efficiency measurements of the photovoltaic solar cells were performed using ORIEL QuantX 300. The photodiode used for the calibration of external quantum efficiency measurements has been calibrated by Newport. The photovoltaic cells were attached to one edge of a LSC using an index-matching polymer adhesive (NOA 68, Norland Products). Black tape was used to cover the area of solar cell exposed outside of the edge. The current density–voltage (*J-V*) characteristics of the LSC/photovoltaic system and c-Si solar cells were measured using a Keithley 2400 sourcemeter under outdoor conditions on a sunny day. The sunlight intensity was around 75 mW cm^{-2} as measured by a Newport calibration meter. The LSC film was perpendicular to the direct beam component of irradiance⁵⁸. For the standard test condition, the *J-V* characteristics were measured under 100 mW cm^{-2} AM 1.5G illumination using a solar simulator (ScienceTech, Class A).

Stability measurements. To characterize thermal stability, we placed LSC films on a hotplate and annealed at 80 °C for 8 h in a N_2 -filled glovebox. The PLQY of the film was measured every hour. To test water stability, LSC films were immersed into deionized water for 8 h. The PLQY of the film was measured every hour.

Continuous illumination photoluminescence stability was acquired by setting the Fluorolog photoluminescence system to an excitation wavelength of 400 nm and utilizing a 4 nm bandpass for the excitation slit. The photoluminescence intensity of film emitted at 500 nm was recorded every 0.5 s. The optical power density is 5 mW cm^{-2} , corresponding to 2.5 mW cm^{-2} absorbed by LSC film, close to the absorbed power density (3 mW cm^{-2}) under outdoor conditions.

For accelerated photoluminescence stability tests, the excitation source was changed to pulsed laser diodes (374 nm, 50 MHz). The power of the laser beam is 1.0 mW with a diameter of 0.1 cm, corresponding to a power density of 127 mW cm^{-2} . After considering the film absorption at 374 nm (50%), this corresponds to an acceleration factor of 20.

GIWAXS measurements. GIWAXS measurements were performed at the Stanford Synchrotron Radiation Lightsources. Two-dimensional scattering data was collected with monochromatic 12.7 keV X-rays and recorded on a Rayonix Mx-225 detector measuring 225 \times 225 mm^2 . Samples were measured in a chamber filled with helium and images were calibrated using LaB₆. Data processing and image manipulation was performed with the MATLAB toolbox GIXSGUI³².

Modelling. The probability of photon out-coupling in Fig. 1 was modelled analytically, assuming realistic material parameters ($k_{\text{rad}} = 1 \text{ ns}^{-1}$, $k_{\text{transfer}} = \{0.1 \text{ ps}^{-1}, k_{\text{rad}}\}$, k_{trap} determined from a PLQY of 70%, $S = 0.1$, $P_{\text{esc}} = 0.25$). Here k_{rad} , k_{transfer} and k_{trap} represent radiative recombination rate, energy transfer rate and non-radiative recombination rate, respectively. P_{esc} represents the probability of a photon escaped from the waveguide. Details on the energy routing model for multilayered perovskite LSCs can be found in Supplementary Methods.

Data availability

The data that support the plots within this paper and other findings of this study are available from the corresponding authors upon reasonable request.

Received: 8 August 2017; Accepted: 7 December 2018;

Published online: 21 January 2019

References

1. Debije, M. G. & Verbunt, P. P. C. Thirty years of luminescent solar concentrator research: solar energy for the built environment. *Adv. Energy Mater.* **2**, 12–35 (2012).
2. Currie, M. J., Mapel, J. K., Heidel, T. D., Goffri, S. & Baldo, M. A. High-efficiency organic solar concentrators for photovoltaics. *Science* **321**, 226–228 (2008).
3. Meinardi, F. et al. Large-area luminescent solar concentrators based on Stokes-shift-engineered nanocrystals in a mass-polymerized PMMA matrix. *Nat. Photon.* **8**, 392–399 (2014).
4. Meinardi, F. et al. Highly efficient luminescent solar concentrators based on earth-abundant indirect-bandgap silicon quantum dots. *Nat. Photon.* **11**, 177–185 (2017).
5. Li, H., Wu, K., Lim, J., Song, H.-J. & Klimov, V. I. Doctor-blade deposition of quantum dots onto standard window glass for low-loss large-area luminescent solar concentrators. *Nat. Energy* **1**, 16157 (2016).
6. Meinardi, F. et al. Highly efficient large-area colourless luminescent solar concentrators using heavy-metal-free colloidal quantum dots. *Nat. Nanotechnol.* **10**, 878–885 (2015).

7. Erickson, C. S. et al. Zero-reabsorption doped-nanocrystal luminescent solar concentrators. *ACS Nano* **8**, 3461–3467 (2014).
8. Wu, K., Li, H. & Klimov, V. I. Tandem luminescent solar concentrators based on engineered quantum dots. *Nat. Photon.* **12**, 105–110 (2018).
9. Sutherland, B. R. & Sargent, E. H. Perovskite photonic sources. *Nat. Photon.* **10**, 295–302 (2016).
10. Tan, Z.-K. et al. Bright light-emitting diodes based on organometal halide perovskite. *Nat. Nanotechnol.* **9**, 687–692 (2014).
11. Nikolaidou, K. et al. Hybrid perovskite thin films as highly efficient luminescent solar concentrators. *Adv. Opt. Mater.* **4**, 2126–2132 (2016).
12. Zhao, H. et al. Perovskite quantum dots integrated in large-area luminescent solar concentrators. *Nano Energy* **37**, 214–223 (2017).
13. Liu, W. et al. Mn²⁺-doped lead halide perovskite nanocrystals with dual-color emission controlled by halide content. *J. Am. Chem. Soc.* **138**, 14954–14961 (2016).
14. Meinardi, F. et al. Doped halide perovskite nanocrystals for reabsorption-free luminescent solar concentrators. *ACS Energy Lett.* **2**, 2368–2377 (2017).
15. Quan, L. N. et al. Ligand-stabilized reduced-dimensionality perovskites. *J. Am. Chem. Soc.* **138**, 2649–2655 (2016).
16. Tsai, H. et al. High-efficiency two-dimensional Ruddlesden–Popper perovskite solar cells. *Nature* **536**, 312–316 (2016).
17. Yuan, M. et al. Perovskite energy funnels for efficient light-emitting diodes. *Nat. Nanotechnol.* **11**, 872–877 (2016).
18. Byun, J. et al. Efficient visible quasi-2D perovskite light-emitting diodes. *Adv. Mater.* **28**, 7515–7520 (2016).
19. Wang, N. et al. Perovskite light-emitting diodes based on solution-processed self-organized multiple quantum wells. *Nat. Photon.* **10**, 699–704 (2016).
20. Xiao, Z. et al. Efficient perovskite light-emitting diodes featuring nanometre-sized crystallites. *Nat. Photon.* **11**, 108–115 (2017).
21. Sichert, J. A. et al. Quantum size effect in organometal halide perovskite nanoplatelets. *Nano Lett.* **15**, 6521–6527 (2015).
22. Weidman, M. C., Seitz, M., Stranks, S. D. & Tisdale, W. A. Highly tunable colloidal perovskite nanoplatelets through variable cation, metal, and halide composition. *ACS Nano* **10**, 7830–7839 (2016).
23. Rowland, C. E. et al. Picosecond energy transfer and multiexciton transfer outpaces Auger recombination in binary CdSe nanoplatelet solids. *Nat. Mater.* **14**, 484–489 (2015).
24. Dou, L. et al. Atomically thin two-dimensional organic-inorganic hybrid perovskites. *Science* **349**, 1518–1521 (2015).
25. Kumar, S. et al. Efficient blue electroluminescence using quantum-confined two-dimensional perovskites. *ACS Nano* **10**, 9720–9729 (2016).
26. Andrew, P. & Barnes, W. L. Förster energy transfer in an optical microcavity. *Science* **290**, 785–788 (2000).
27. Baldo, M. A., Thompson, M. E. & Forrest, S. R. High-efficiency fluorescent organic light-emitting devices using a phosphorescent sensitizer. *Nature* **403**, 750–753 (2000).
28. Crooker, S. A., Hollingsworth, J. A., Tretiak, S. & Klimov, V. I. Spectrally resolved dynamics of energy transfer in quantum-dot assemblies: towards engineered energy flows in artificial materials. *Phys. Rev. Lett.* **89**, 186802 (2002).
29. Medintz, I. L., Uyeda, H. T., Goldman, E. R. & Mattoussi, H. Quantum dot bioconjugates for imaging, labelling and sensing. *Nat. Mater.* **4**, 435–446 (2005).
30. Meinardi, F., Bruni, F. & Brovelli, S. Luminescent solar concentrators for building-integrated photovoltaics. *Nat. Rev. Mater.* **2**, 17072 (2017).
31. Klimov, V. I. et al. Quality factor of luminescent solar concentrators and practical concentration limits attainable with semiconductor quantum dots. *ACS Photon.* **3**, 1138–1148 (2016).
32. Song, H.-J. et al. Performance limits of luminescent solar concentrators tested with seed/quantum-well quantum dots in a selective-reflector-based optical cavity. *Nano Lett.* **18**, 395–404 (2018).

Acknowledgements

This publication is based in part on work supported by the US Department of the Navy, Office of Naval Research (Grant Award No. N00014-17-1-2524), the Ontario Research Fund Research Excellence Program, and by the Natural Sciences and Engineering Research Council (NSERC) of Canada. L.N.Q. acknowledges the financial support by National Research Foundation of Korea Grant funded by the Korean Government (2014R1A2A1A09005656; 2015M1A2A2058365). F.P.G.d.A. acknowledges financial support from the Connaught fund. A.G.-P. is supported by NSF GRFP (DGE-1147470). Use of the Stanford Synchrotron Radiation Lightsource, SLAC National Accelerator Laboratory, is supported by the US Department of Energy, Office of Science, Office of Basic Energy Sciences under Contract No. DE-AC02-76SF00515.

Author contributions

M.W., F.P.G.d.A. and G.W. contributed equally to this work. M.W., F.P.G.d.A., Z.Y. and E.H.S. conceived the idea and proposed the experimental and modelling design. F.P.G.d.A. performed the simulation and directed the experiments. M.W., L.N.Q. and Y.K. synthesized the materials and fabricated the devices. M.W. and G.W. performed the measurements. M.W. and R.S. conducted the transient absorption measurements. M.W., L.G. and G.W. performed stability test. G.W., F.F. and M.W. carried out AFM and TEM measurements. R.Q.-B., A.G.-P. and M.F.T. were responsible for the GIWAXS measurements. M.W., F.P.G.d.A., G.W. and E.H.S. co-wrote the manuscript. All authors contributed in data analysis, read and commented on the manuscript.

Competing interests

The authors declare no competing interests.

Additional information

Supplementary information is available for this paper at <https://doi.org/10.1038/s41560-018-0313-y>.

Reprints and permissions information is available at www.nature.com/reprints.

Correspondence and requests for materials should be addressed to E.H.S.

Publisher's note: Springer Nature remains neutral with regard to jurisdictional claims in published maps and institutional affiliations.

© The Author(s), under exclusive licence to Springer Nature Limited 2019